

Global extreme heat forecasting using neural weather models

Ignacio Lopez-Gomez,^{a,b} Amy McGovern,^{a,c} Shreya Agrawal,^a Jason Hickey,^a

^a *Google Research, Mountain View, California*

^b *California Institute of Technology, Pasadena, California*

^c *University of Oklahoma, Norman, Oklahoma*

arXiv:2205.10972v1 [physics.ao-ph] 23 May 2022

Corresponding author: Ignacio Lopez-Gomez, ilopezgo@caltech.edu

ABSTRACT: Heat waves are projected to increase in frequency and severity with global warming. Improved warning systems would help reduce the associated loss of lives, wildfires, power disruptions, and reduction in crop yields. In this work, we explore the potential for deep learning systems trained on historical data to forecast extreme heat on short, medium and subseasonal timescales. To this purpose, we train a set of neural weather models (NWMs) with convolutional architectures to forecast surface temperature anomalies globally, 1 to 28 days ahead, at ~ 200 km resolution and on the cubed sphere. The NWMs are trained using the ERA5 reanalysis product and a set of candidate loss functions, including the mean squared error and exponential losses targeting extremes. We find that training models to minimize custom losses tailored to emphasize extremes leads to significant skill improvements in the heat wave prediction task, compared to NWMs trained on the mean squared error loss. This improvement is accomplished with almost no skill reduction in the general temperature prediction task, and it can be efficiently realized through transfer learning, by re-training NWMs with the custom losses for a few epochs. In addition, we find that the use of a symmetric exponential loss reduces the smoothing of NWM forecasts with lead time. Our best NWM is able to outperform persistence in a regressive sense for all lead times and temperature anomaly thresholds considered, and shows positive regressive skill compared to the ECMWF subseasonal-to-seasonal control forecast within the first two forecast days and after two weeks.

SIGNIFICANCE STATEMENT: Heat waves are projected to become stronger and more frequent as a result of global warming. Accurate forecasting of these events would enable the implementation of effective mitigation strategies. Here we analyze the skill of artificial intelligence systems trained on historical surface temperature data to predict extreme heat events globally, 1 to 28 days ahead. We find that artificial intelligence systems trained to focus on extreme temperatures have significantly higher skill than systems trained to minimize errors in surface temperatures, and remain equally skillful at predicting moderate temperatures. Furthermore, the extreme-focused systems compete with state-of-the-art physics-based forecast systems in the subseasonal range, while incurring a much lower computational cost.

1. Introduction

An important consequence of anthropogenic radiative forcing is the robust increase in heat wave days per year, both globally and at a regional level (Perkins-Kirkpatrick and Lewis 2020). Heat waves pose a significant health risk, evinced by the more than 70,000 excess deaths that occurred during the 2003 European heat wave (Robine et al. 2008). More frequent heat waves will also lead to higher wildfire risk (Parente et al. 2018; Ruffault et al. 2020), stress on the power grid (Ke et al. 2016), and loss of agricultural crops (Brás et al. 2021). These trends underscore the importance of developing effective mitigation strategies to reduce the negative impacts of extreme heat. A stepping stone in the development of such strategies are accurate forecasts with sufficient lead time (Lin et al. 2022). Current physics-based models, however, can only provide accurate forecasts a few days in advance, which may not be sufficient to deploy effective mitigation strategies (White et al. 2017; Wulff and Domeisen 2019).

There is mounting evidence of heat wave predictors on weekly to subseasonal timescales. These include large-scale quasi-stationary atmospheric Rossby waves (Teng et al. 2013; Mann et al. 2018; White et al. 2021), negative soil moisture anomalies (Vautard et al. 2007; Benson and Dirmeyer 2021), and anomalous Pacific sea surface temperature (SST) gradients in the case of North American heat waves (Deng et al. 2018; Miller et al. 2021). Recently, Miller et al. (2021) used a linear regression model based on empirical orthogonal functions of the North Pacific SST and soil moisture over the United States to predict the weekly frequency of extremely warm days in the United States, 1 to 4 weeks ahead. They show that their statistical model outperforms the

operational NCEP CFSv2 model in this task over the eastern United States after the second week, which suggests that purely data-driven forecasting may provide a path forward in extreme heat prediction beyond the 10-day horizon.

In this context, deep neural networks represent a natural extension of the data-driven approach, given their remarkable success in image segmentation and forecasting tasks (Ronneberger et al. 2015; Sønderby et al. 2020; Ravuri et al. 2021). Different methods to classify heatwaves leveraging deep learning have recently been proposed. Chattopadhyay et al. (2020) trained a capsule neural network on midtropospheric geopotential and surface temperature from a large ensemble of climate model runs to classify several future days into 5 different classes, each representing either a specific heat wave pattern over North America, or the absence of extreme temperatures. Jacques-Dumas et al. (2022) trained a convolutional neural network on wavenumber space to forecast the occurrence of heat waves in France with a 15-day lead time. They used the same predictors as Chattopadhyay et al. (2020), and data from a 1000-year cyclic climate model simulation.

These studies showcase the potential of deep learning to forecast extreme heat events as a classification problem, in particular regions, and trained on very large datasets sampled from quasi-stationary distributions. Here, we tackle some of the practical questions left unanswered by previous work:

- Can deep learning models forecast extreme heat events when trained on limited historical data? The use of observations or reanalysis data is crucial for systems to improve upon existing physics-based models, since deep learning models trained solely on synthetic data will at best inherit the biases of the numerical simulators they are trying to substitute.
- Can general purpose neural weather models (NWMs) be used to predict extreme heat events? By general purpose, we refer to deep learning systems trained to minimize errors in the underlying fields, such as temperature, and not on extreme classification explicitly (e.g., Rasp et al. 2020; Weyn et al. 2020; Pathak et al. 2022; Keisler 2022). These may be thought of as the data-driven equivalent of physics-based weather models.
- Can NWMs improve their extreme prediction skill through the use of custom losses, while retaining their skill in a general weather forecasting setting?

To answer these questions, we frame extreme heat prediction as a regression problem and restrict our training data to a large subset of the ERA5 reanalysis product. Framing the forecast problem as a regression task bridges the gap with NWMs that act as time integrators, and require reliable previous forecasts as inputs to generate a new prediction (e.g., Brenowitz and Bretherton 2018; Weyn et al. 2020). The regression problem is also more robust to the definition of heat waves, diverse in the literature (e.g., Chattopadhyay et al. 2020; Wulff and Domeisen 2019; Miller et al. 2021), and allows learning about the nuances of target states that may otherwise be masked under the same class in a classification problem. The advent of skillful regression-based NWMs would democratize ensemble-based weather forecasting, which requires enormous computational resources when realized through state-of-the-art physics-based models (Palmer 2017). In contrast, deep learning systems only incur high computational costs during training, but not during inference (Scher and Messori 2021; Weyn et al. 2021).

To address the second question, we make use of state-of-the-art convolutional architectures on the cubed sphere, following Weyn et al. (2020), so that results can be extrapolated to similar NWMs described in the literature. Finally, to explore the last question, we compare forecasts of NWMs trained with the general purpose mean squared error loss to forecasts from NWMs trained to minimize custom losses that emphasize extremes. All results presented are contextualized through comparison with the ECMWF S2S operational forecast system.

The paper is organized as follows. In Section 2, we define the forecasting task and describe the data and losses used to train the NWMs. In Section 3, the model architecture is discussed. Section 4 explores the skill of NWMs trained using different loss functions in tasks varying from extreme heat to general surface temperature prediction, including example forecasts for the 2017 Iberian heatwave and the 2021 western North American heatwave. In Section 5, the relevance of the different NWM inputs is explored using integrated gradients (Sundararajan et al. 2017). Finally, Section 6 ends with a discussion of the results and potential future research directions.

2. The forecasting problem

The forecasting task, given a set of observed input and target pairs (x, y) with $y \in \Omega \subset \mathbb{R}^d$ and $x \in V \subset \mathbb{R}^q$, can be framed as the following minimization problem,

$$\theta^* = \arg \min_{\theta} \int_{\Omega} L(\Psi(\theta, x), y) dy, \quad (1)$$

where $\Psi : \mathbb{R}^p \times \mathbb{R}^q \rightarrow \mathbb{R}^d$ is a mapping from parameter and input space to target space, $\theta \in \mathbb{R}^p$ are model parameters, $x \in \mathbb{R}^q$ is an input data vector, and $L(\cdot, \cdot)$ is some loss that we seek to minimize over a target set $\Omega \subset \mathbb{R}^d$. In this paper, we consider Ψ to be a convolutional neural network operating on a gnomonic equiangular cubed sphere, described in detail in Section 3. Two-dimensional convolutions are performed on each face of the cubed sphere using halo exchange between faces, following the approach of Weyn et al. (2020). Architecture exploration for NWMs is an active area of research (Pathak et al. 2022; Keisler 2022), but this is not the emphasis of this work, so we keep the architecture Ψ fixed. Instead, we are interested in comparing the usefulness of NWMs $\Psi(\theta^*, \cdot)$ that result from the minimization (1) when varying the definition of the loss. Finally, the NWM parameter vector θ^* given a loss definition is obtained through mini-batch gradient descent, using the Adam algorithm (Kingma and Ba 2017).

a. Data, predictors and targets

The targets y are constructed from the daily average of the standardized climatological anomalies of the temperature 2 m above the surface (T_{2m}), which we denote \tilde{T}_{2m} . We recognize that air temperature is a suboptimal indicator of heat-related illness (Xu et al. 2016; Heo et al. 2019), but it enables comparison with other physics-based and neural weather models in the literature (Weyn et al. 2021; Wulff and Domeisen 2019; Lin et al. 2022). Each target vector y includes \tilde{T}_{2m} for a set of lead times $\tau = 1, \dots, \tau_f$ days and for all tiles of a gnomonic equiangular grid of Earth’s surface (Ronchi et al. 1996). Thus, the target size d is the flattened length of the tensor $y_{cs} \in \mathbb{R}^{\tau_f \times f \times h \times w}$, where $f = 6$ is the number of faces of the cubed sphere, and $h = 48$ and $w = 48$ are the number of meridional and zonal tiles of each face, respectively. The cubed sphere grid we employ is shown in Figure 1 for reference; the surface area of each tile is approximately 192^2 km^2 . To assess the skill

of the model from the short to the subseasonal range, we aim to predict temperature anomalies for the next $\tau_f = 28$ days.

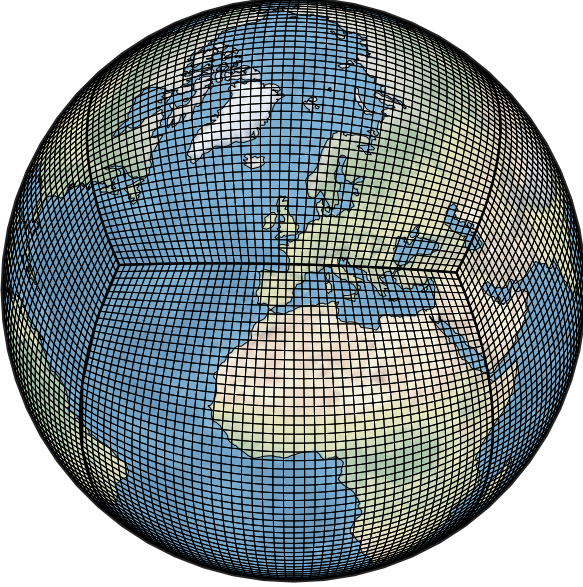


FIG. 1. Depiction of the gnomonic cubed sphere grid onto which predictors and targets are projected. The cubed sphere is composed of 6 faces with $48^2 = 2304$ cells each.

The input data vectors $x \in V \subset \mathbb{R}^q$ contain v daily-averaged surface fields on the cubed sphere. For time-dependent fields, past times $\tau = 1 - \tau_p, \dots, 0$ days are included in x , such that q is the flattened length of the tensor $x_{cs} \in \mathbb{R}^{v \times f \times h \times w}$. Here $v = \tau_p v_t + v_i$ is the number of input fields, $\tau_p = 7$ days and v_t, v_i are the number of time-dependent and independent fields, respectively. We consider as time-dependent input fields the geopotential height and potential vorticity at 300, 500 and 700 hPa, the temperature T_{2m} , the mean top net long-wave radiative flux (OLR), the volume of water in soil layers 0 – 7 cm, 7 – 28 cm, 28 – 100 cm and 100 – 289 cm, the insolation and the date. To these fields we append as auxiliary time-independent variables the latitude, longitude, topography and a land-sea mask. The full list of predictors is summarized in Table 1.

The choice of predictors is informed by studies linking extreme heat events to mid-tropospheric geopotential height (Teng et al. 2013; Mann et al. 2018; Chattopadhyay et al. 2020), soil moisture (Vautard et al. 2007; Miller et al. 2021; Benson and Dirmeyer 2021) and large-scale phenomena with a characteristic outgoing longwave radiation signature, like the Madden-Julian Oscillation

(Jacques-Coper et al. 2015; Maloney et al. 2019) or the Boreal summer intraseasonal oscillation (Lin et al. 2022). In addition, we include T_{2m} to learn about transport processes such as advection; and its standardized anomaly to facilitate improving upon the predictive skill of a persistence model. Both T_{2m} and \tilde{T}_{2m} capture the signature of large-scale oscillations such as El Niño (ENSO) or the North Atlantic Oscillation (Ogi et al. 2003; Wang et al. 2011; Wright et al. 2014).

TABLE 1. Predictors used for the temperature anomaly prediction task. Anomalies are standardized (std.) with respect to climatology. Heights are specified as above (a.g.) and below (b.g.) ground level.

Predictor	Levels
Temperature anomaly (std.)	2 m (a.g.)
Temperature	2 m (a.g.)
Geopotential height anomaly (std.)	300, 500, 700 hPa
Geopotential height	300, 500, 700 hPa
Potential vorticity anomaly (std.)	300, 500, 700 hPa
Potential vorticity	300, 500, 700 hPa
Outgoing longwave radiation	Top of atmosphere
Incoming shortwave radiation	Top of atmosphere
Surface soil moisture	0 – 7, 7 – 28 cm (b.g.)
Deep soil moisture	28 – 100, 100 – 289 cm (b.g.)
Topography	N/A
Land-sea mask	N/A
Latitude, longitude	N/A
Date	N/A

All data are daily averages from the ERA5 reanalysis product (Hersbach et al. 2020), downloaded at $2^\circ \times 2^\circ$ resolution and projected onto the cubed sphere. The climatologies are computed for the time period 1979 – 2019, and projection onto the cubed sphere is performed following Ullrich and Taylor (2015); Ullrich et al. (2016). All days of the year, not only the summer days, are used to train the model. We do this to learn about physical processes driving temperature anomalies that are not season dependent, like advection. When framed as a classification task, extreme heat prediction may require undersampling of non-extreme samples when training the model (Jacques-Dumas et al. 2022). Here, we make use of all available information with no explicit undersampling; class imbalance is dealt with through the use of custom losses as discussed in Section 2b. In addition, we perform a strictly sequential split of the data into training (1979-2012), validation (2013-2016) and test sets (2017-2021). A shift in the target distribution from training to testing sets is implicit

with this split, due to climate change (White et al. 2021). This shift is, however, representative of situations in which a warning system might be used in practice.

b. Losses considered

Unless the optimal parameter vector θ^* is able to yield a perfect model (i.e., $\Psi(\theta^*, x) = y \ \forall (x, y)$), the optimum will depend on the definition of the loss $L : \mathbb{R}^d \times \mathbb{R}^d \rightarrow \mathbb{R}$. This is the case in the extreme heat prediction task, since the chaotic nature of the atmosphere precludes a perfect forecast of trajectories from inexact initial conditions (Lorenz 1969a,b; Slingo and Palmer 2011). For this reason, we can expect models that minimize generic losses to be suboptimal for the extreme prediction task.

To study the potential benefits of training NWMs on losses targeting extreme prediction, we consider two losses: the generic mean squared error (MSE) and a custom loss L_e based on the exponential of targets and forecasts,

$$L_e(y', y) = a\text{MSE}(e^{y'}, e^y) + b\text{MSE}(e^{-y'}, e^{-y}), \quad (2)$$

where y are the targets and y' are the forecasts. In equation (2), the choice $(a, b) = (1, 0)$ emphasizes the correct prediction of positive extremes, $(a, b) = (0, 1)$ the model skill for negative extremes, and the midpoint $(a, b) = (0.5, 0.5)$ emphasizes both extremes. In the context of temperature anomaly prediction, these losses emphasize heat waves, cold spells and extreme deviations from climatology, respectively. This custom loss definition is motivated by the reported success of neural networks in extreme prediction tasks when using target transformations involving the softmax and softmin functions (Qi and Majda 2020). However, we exclusively take the numerator of the suggested transformations because the softmax and softmin functions are invariant under translational shifts (Appendix A, Lopez-Gomez et al. 2020), which in this application means that climatological biases would not be penalized.

In the following, we denote models trained with the loss (2) as HeatNet for $(a, b) = (1, 0)$ and ExtNet for $(a, b) = (0.5, 0.5)$. These are models trained for the extreme heat forecasting task and the symmetric extreme prediction task, respectively. The model trained with the generic mean squared error loss, representative of general neural weather prediction systems (e.g., Rasp et al. 2020; Weyn et al. 2020, 2021), is denoted GenNet.

We trained HeatNet, ExtNet and GenNet models using a hyperparameter search over the learning rate, and the magnitude of L_1 and L_2 regularization. All models were trained until they started overfitting to the training set, evidenced by an increase in validation loss persistent over many epochs. Notably, our best HeatNet and ExtNet models in terms of validation loss were obtained by retraining our best GenNet model for a few (< 3) epochs on the custom exponential loss. This implies that any performance improvements of HeatNet or ExtNet with respect to generic models trained on the MSE loss can be realized efficiently through transfer learning from the original models.

3. Neural weather model architecture

We employ a non-recurrent convolutional architecture to construct the neural network Ψ , which maps the input fields at all past times $\tau = -6, \dots, 0$ days to the daily-averaged temperature anomaly \tilde{T}_{2m} at all lead times $\tau = 1, \dots, 28$ days. Consistent with our projection of the data, convolutions are performed on each of the cubed sphere faces, using halo exchange at the borders (Weyn et al. 2020). Kernel weights are shared among all 4 equatorial faces, and a different set of kernel weights is used for the polar faces. This enables learning about different processes governing on one hand tropical and subtropical dynamics, and on the other mid- and high-latitude dynamics. The northern polar face is mirrored before each convolution to align cyclonic and anticyclonic motions in each hemisphere, following Weyn et al. (2020).

a. Receptive field

Due to the non-recurrent nature of the architecture and the lead times considered, it is crucial to achieve a fully receptive field if we want to capture possible long-range dependencies and teleconnections (Espeholt et al. 2021). A fully receptive field is realized through two design characteristics of the proposed architecture, which is sketched in Figure 2. The first one is the use of exponentially dilated convolutions, which rapidly increase the receptive field of any location on the cubed sphere as information traverses the network (Yu and Koltun 2016). The second one is the use of a UNet-type architecture (Ronneberger et al. 2015) with 3 resolution levels going from the data resolution to the synoptic scale: $\sim 200^2$, $\sim 400^2$ and $\sim 800^2$ km². Coarser-resolution levels

increase the receptive field proportionally to their downsampling rate, allowing to achieve larger receptive fields with fewer layers.

b. Encoder and decoder architecture

The architecture of our model is based on the UNet 3+ architecture (Huang et al. 2020) with a few modifications. All nonlinearities consist of PReLU activations that share parameters across all dimensions except the channels (He et al. 2015). We use dilated convolutions, as previously mentioned, with exponentially-growing dilation factors f_d that increase with network depth at every resolution level. The first two levels have encoder and decoder stacks with 2 layers each, while the synoptic-scale level is composed of an encoder stack with 4 layers.

Each encoder layer $l = 0, 1, \dots$ applies 2D 3×3 dilated convolutions with dilation factor $f_d = 2^l$ and a PReLU nonlinearity. The decoder layers in the first two levels apply 2D 3×3 convolutions with dilation factors $f_d = 2^3, 2^4$, and are each followed by a PReLU nonlinearity. In addition, we include a nonlinear skip connection at the finest resolution level to easily capture persistence. Downsampling between levels is performed using max-pooling, although models using average-pooling demonstrated similar skill in our study (not shown). In the decoder, upsampling is followed by 2D 3×3 convolutions. The number of layers per level was obtained through cross-validation from a small set of architectures that achieved a full receptive field.

All layers at 200^2 km^2 are composed of 32 convolutional filters, and layers at 400^2 km^2 and 800^2 km^2 resolution apply 64 and 128 filters to their inputs, respectively. The skip connections between encoder and decoder stacks, as well as the upsampling layers, have 32 filters each. In each layer of the network, we use two independent convolutional kernels for each filter: one covering all 4 equatorial faces of the cubed sphere, and the other covering the polar faces. As shown in Section 4, there is no discernible imprint of the cubed sphere edges on the model forecasts. In the end, the model architecture has about 1.8 million parameters, halfway between the complexity of the models used in Weyn et al. (2020) and Weyn et al. (2021).

4. Results

We assess the skill of models trained on the exponential and generic losses (i.e., HeatNet, ExtNet and GenNet) against persistence and the European Centre for Medium-Range Weather Forecasts

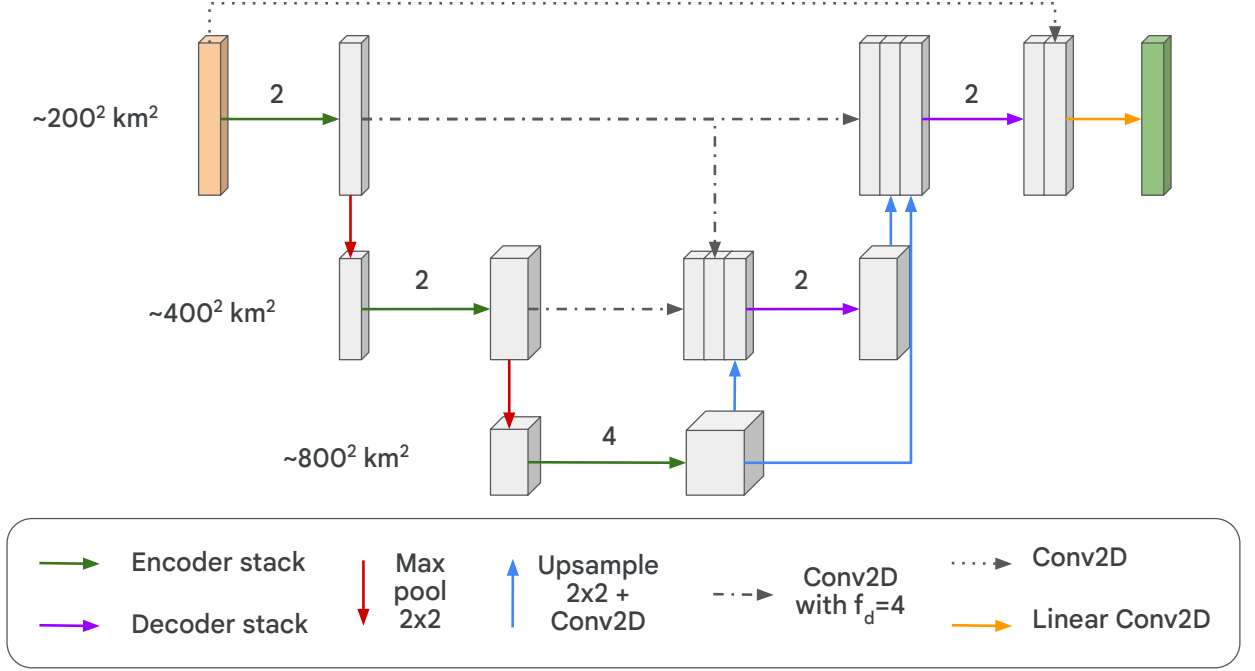


FIG. 2. Neural weather model architecture, modified from a UNet 3+ architecture (Huang et al. 2020). The number of layers of each encoder and decoder stack are as indicated in the schematic. Encoder convolutional layers have exponentially-growing dilation factors $f_d = 2^l$, where $l = 0, 1, \dots$ is the layer number within the stack from inputs to outputs, and decoder layers have dilation factors $f_d = 8$ and 16. The layers connecting same-level encoders and decoders have convolutions with $f_d = 4$ and 32 filters. All other layers have dilation factor $f_d = 1$, and all layers have convolutional kernels of size 3×3 . Same-level layers implement 32, 64 and 128 filters in the first, second and third levels, respectively.

(ECMWF) subseasonal-to-seasonal (S2S) forecast system (Vitart et al. 2017). The ECMWF S2S system is a state-of-the-art operational model that provides real-time 46-day forecasts twice a week. For dates in the test set (2017 – 2021), real-time forecasts used ECMWF’s IFS cycles CY43R1, CY46R1 and CY47R2 (ECMWF 2016, 2019, 2020). These model versions have a horizontal resolution of $0.25^\circ \times 0.25^\circ$ for days 1 – 10, and $0.5^\circ \times 0.5^\circ$ after that. The S2S model employed 91 vertical levels in the atmosphere until May 2021, and 137 levels after the implementation of the CY47R2 cycle. All cycle versions are coupled to an ocean model at $0.25^\circ \times 0.25^\circ$ resolution with an interactive sea-ice model.

In order to compare against our deep learning systems, the ECMWF forecasts are coarse-grained to the same resolution as the input ERA5 data ($2^\circ \times 2^\circ$), subtracting the same climatology. Then, the results are mapped to be cubed sphere, where all skill metrics are computed. For all comparisons in this study, we employ both the real-time daily averaged ECMWF control and perturbed ensemble forecasts (Vitart et al. 2017). Comparisons with the ECMWF control assess the skill of the neural weather model against a deterministic "best-guess" physics-based forecast. Operational warning systems typically use perturbed ensembles, which have been shown to yield a higher economic value than a single high-resolution deterministic forecast (Richardson 2000; Palmer 2017). For this reason, we include the ECMWF ensemble mean forecast for comparison, even though our models yield a single deterministic output.

Although we compare forecast skill for the same dates, the real-time ECMWF S2S system is initialized from the operational IFS analysis, not ERA5. This should be considered when interpreting the relative skill of the ECMWF model during the first few lead time days. Model drift is removed from the real-time ECMWF forecasts during the post-processing stage, using a total of 660 reforecast integrations covering the climatology of the past 20 years and initialized from ERA5 data (Vitart et al. 2017).

a. Forecast skill for summer over land

Although we train the NWMs using global data from all seasons, we evaluate here the performance of the forecast systems exclusively for summer over land, where heat wave prediction is most relevant. We define summer as the June-July-August trimester for the Northern Hemisphere and December-January-February for the Southern Hemisphere.

To assess model skill during increasingly hot summer days, we consider forecasts for which the true ERA5 targets were above two different temperature anomaly thresholds: 1 standard deviation and 2 standard deviations above the 1979-2019 daily climatology. Setting these thresholds also allows assessing the forecast systems as binary classifiers. The regressive skill of the models is characterized in this study through two metrics: the debiased root mean squared error of standardized temperature anomalies (RMSE_d) and the \tilde{T}_{2m} centered anomaly correlation coefficient (AnCC). The RMSE_d is defined as the RMSE of forecasts with respect to targets after removing the global mean bias per lead time of forecasts and targets in the test set. We choose to debias

the forecasts to prevent forecast bias from positively affecting the skill metric, since the mean target above the temperature thresholds is nonzero. The subtracted bias is shown for all models in Figure 5 for reference. The RMSE_d can be further interpreted as the RMSE of the dynamic temperature anomalies, after the predicted global mean thermodynamic shift in temperatures has been subtracted.

The centered anomaly correlation coefficient for a given lead time i is defined as (Wulff and Domeisen 2019)

$$\text{AnCC}_i = \frac{\sum_{k=1}^{N_i} (y_{ik} - \bar{y}_i)(y'_{ik} - \bar{y}'_i)}{\sqrt{\sum_{k=1}^{N_i} (y_{ik} - \bar{y}_i)^2 \sum_{k=1}^{N_i} (y'_{ik} - \bar{y}'_i)^2}}, \quad (3)$$

where $\bar{y}_i \in \mathbb{R}$ is the temporal and spatial average of the target temperature anomaly \tilde{T}_{2m} at lead time i for summer over land over the entire test set; $y_{ik} \in \mathbb{R}$ are individual values of \tilde{T}_{2m} at lead time i and at a given location and summer day, indexed by k ; and the sums are over the N_i summer targets y_{ik} above the considered standardized temperature anomaly threshold. The forecast counterparts \bar{y}'_i and y'_{ik} are defined similarly based on the forecast temperature anomaly, but the sum over indices k is still conditioned on the anomaly threshold of the targets. The AnCC is a useful metric of the potential of a forecast system, measuring the correlation between the target and forecast outputs (Chapter 9, Wilks 2019). Our centered definition (3) takes into account the dynamic temperature anomalies, filtering out the thermodynamic shift of temperature anomalies over land with respect to the 1979-2019 climatology due to global warming, as well as lead-time dependent model biases. This is not the case for the non-centered anomaly correlation coefficient, which does not filter out forecast biases with respect to climatology (e.g., Weyn et al. 2020).

The classification skill of the models is evaluated through the extremal dependence index (EDI, Ferro and Stephenson 2011) and the equitable threat score (ETS). The EDI is defined as

$$\text{EDI} = \frac{\log F - \log H}{\log F + \log H}, \quad H = \frac{a}{a+c}, \quad F = \frac{b}{b+d}. \quad (4)$$

where F is the false alarm rate, H is the hit rate, a are the hits, b are the false alarms, c are the misses, and d the correct negatives (Wilks 2019). Positive values of EDI indicate higher skill than a random forecast. We choose this metric because it is base-rate independent, equitable, and it does not degenerate for rare event classifiers. Thus, the EDI between both thresholds considered

can be compared, which is not the case for base-rate dependent measures (Wulff and Domeisen 2019). The more widely used equitable threat score is defined as

$$\text{ETS} = \frac{\text{TS} - \text{TS}_{\text{ref}}}{1 - \text{TS}_{\text{ref}}}, \quad \text{TS} = \frac{a}{a + b + c}, \quad (5)$$

where TS_{ref} is the threat score of a random forecast, and higher ETS is representative of higher skill.

The skill of the different models over land is shown in Figure 3 for the summers of 2017-2021. The lead time is shown in a logarithmic scale to differentiate between three different time scales: the short range (≤ 3 days), the medium range (4 – 10 days), and the extended or subseasonal range (11 – 28 days). In the short range errors are dominated by the initialization, which is more precise for the NWMs, since ERA5 data are fed as predictors. The medium range is characterized by predictable trajectories of the atmospheric state, whereas forecasting a single trajectory in the extended range typically adds little value over climatology (Lorenz 1969b). Predictive power in the subseasonal range is typically associated with controlling factors involving slower dynamical systems, like the ocean (Palmer 1993).

The extreme-focused HeatNet and ExtNet outperform GenNet for both temperature thresholds and all metrics considered, highlighting the usefulness of the exponential loss (2) in the extreme prediction task. All NWMs maintain a higher anomaly correlation with the targets than persistence, but only the model trained on the symmetric exponential loss improves upon persistence in a mean squared error sense during extremely hot days ($\tilde{T}_{2m} > 2$). HeatNet, which is trained to emphasize positive extremes exclusively, yields forecasts with higher AnCC than the symmetric ExtNet during hot summer days. Although the AnCC difference indicates higher predictive potential compared to ExtNet in this task, its one-sided emphasis on heatwaves leads to a significant positive bias, as shown in Figures 4 and 5. This bias is detrimental to the prediction of dynamic temperature anomalies, increasing the RMSE_d , and does not lead to significant classification skill improvements over ExtNet (EDI, ETS in Figure 3).

All NWMs outperform the physics-based models in the short range, due to initialization improvements that may not be fully realizable in a real-time setting. In the medium range, the control and ensemble ECMWF forecasts remain superior, but their skill drops significantly faster than that of the NWMs beyond 10 days of lead time. After the second week, the extreme-focused NWMs

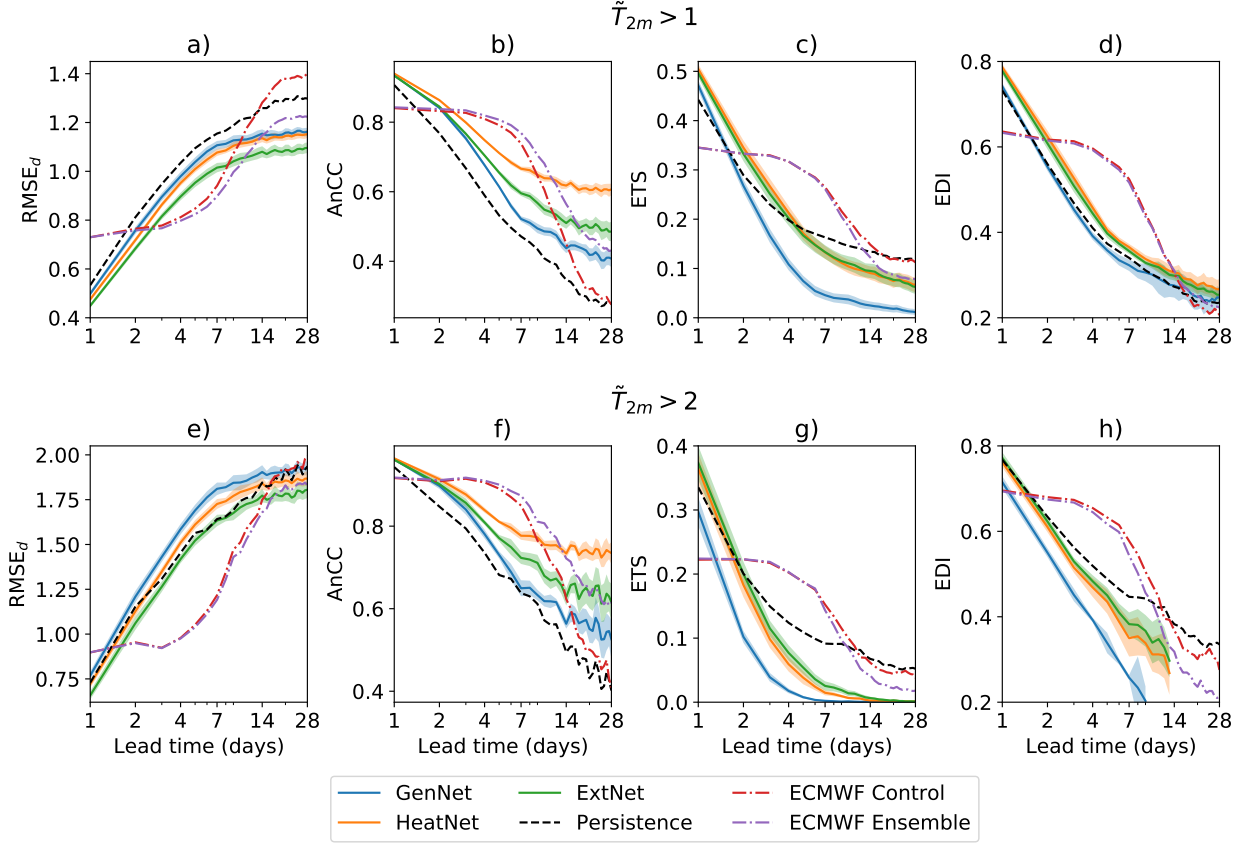


FIG. 3. Forecast metrics for different models during the summer months of 2017-2021 and over land. Metrics are shown for forecasts conditioned on target temperature anomalies being above 1 (top) and 2 (bottom) standard deviations from climatology. From left to right, the debiased root mean squared error ($RMSE_d$), centered anomaly correlation coefficient (AnCC), equitable threat score (ETS) and extremal dependence index (EDI) are shown. Uncertainty bands, shown for the NWMs as a reference, represent 1 standard deviation. Results are only shown for metrics with a robust uncertainty estimate; details may be found in Appendix A. For reference, the climatological $RMSE_d$ is higher than 1.2 for $\tilde{T}_{2m} > 1$ and 2.1 for $\tilde{T}_{2m} > 2$, above the $RMSE_d$ of all NWMs.

(ExtNet and HeatNet) have higher regressive skill than the control physics-based model both in terms of $RMSE_d$ and correlations with the true anomalies. The $RMSE_d$ skill of NWMs relative to the ECMWF system is significantly higher when considering all hot days ($\tilde{T}_{2m} > 1$) than during extremely hot days ($\tilde{T}_{2m} > 2$). Both ExtNet and HeatNet show positive skill relative to the ECMWF ensemble in the less extreme task; during extremely hot days their skill only becomes comparable to the ECMWF ensemble after the third week. Positive skill in the extended range is enabled by

the use of the exponential loss, without which the neural weather model is unable to compete with the operational system beyond the short range.

The ECMWF ensemble mean forecast substantially improves upon the regressive skill of the control run in the extended range, with RMSE_d and AnCC metrics closer to ExtNet. However, higher regressive skill in the extended range does not translate into higher classification skill, as shown by the ETS and EDI diagnostics. As classifiers, HeatNet and ExtNet have similar skill to the ECMWF ensemble beyond the medium range for hot ($\tilde{T}_{2m} > 1$) days, scoring higher on EDI but lower on ETS. During extremely hot ($\tilde{T}_{2m} > 2$) days, all NWMs fail to improve upon persistence or the ECMWF system as classifiers, although the use of exponential losses increases the skill of the NWMs for all regression and classification metrics considered.

b. Predictability of increasingly hot summer days

It is interesting to note that most models considered, including persistence, show a higher AnCC and EDI for more extreme events. This has been documented before by Wulff and Domeisen (2019), who attribute this apparent increase in predictability to slowly-varying flow patterns and land-atmosphere interactions that precede heat waves. The fact that a similar increase in AnCC and EDI is also seen for persistence unfortunately suggests that this may just be due to the fact that stronger heat waves are longer-lived; it does not necessarily point to longer lead time predictability of heat wave initiation with respect to persistence.

c. Smoothing of forecasts with lead time

The contrast between regressive and classifying skill of NWMs and the ECMWF ensemble is due to a smoothing of their forecasts as lead time progresses, and the predictability of the targets diminishes. Here, we define smoothing as loss of sharpness, or loss of ability to predict events far from climatology. This smoothing is illustrated in Figure 4 through the evolution of the forecast probability density functions (PDFs) with lead time for all models considered. Smoothing leads to a density concentration near the mean, as the probability of strong temperature anomalies decreases.

In the case of the ECMWF ensemble, lower predictability reduces the correlation between individual forecasts with lead time. This leads to a variance reduction in the ensemble mean distribution. Smoothing is also typical of data-driven methods, although in this case it is the result

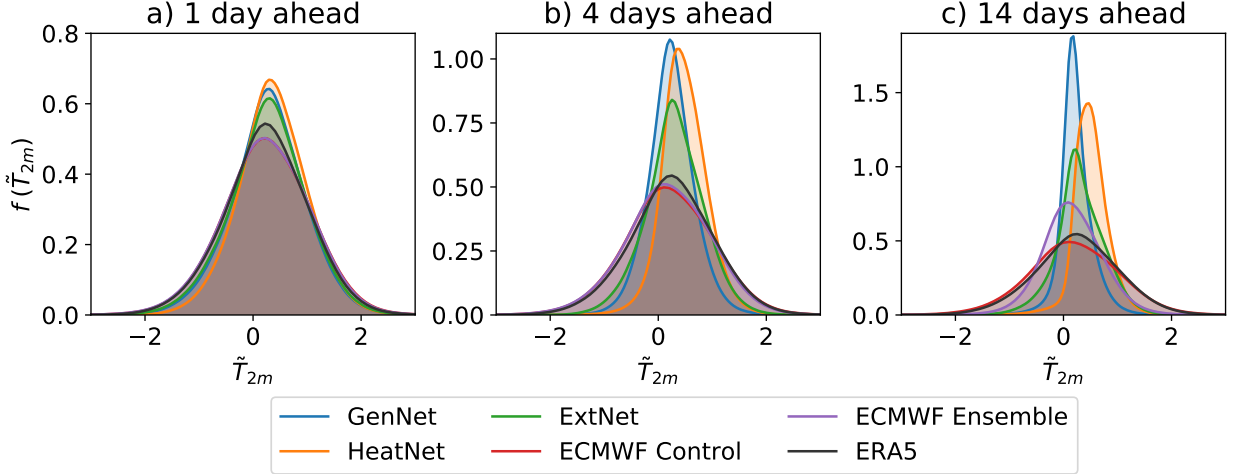


FIG. 4. Probability density functions (PDFs, here $f(\cdot)$) of forecast global standardized temperature anomalies during the period 2017-2021. Results are shown for all NWMs, the control and ensemble forecasts from the ECMWF S2S system, and the true target distribution (ERA5). Note that the PDFs are not centered about zero, indicating a prediction of the shift in climatology from the 1979-2019 mean.

of forecast error minimization under uncertainty (e.g., Sønderby et al. 2020). While the PDF of individual (hindcast-corrected) physics-based forecasts remains relatively constant, data-driven forecasts shift towards distributions closer to the target mean, with fewer extreme events.

Notably, this smoothing is slowed down through the use of the exponential loss (2), particularly in ExtNet. The use of the symmetric exponential loss increases the probability of significant deviations from climatology. Minimizing the positive exponential loss also reduces forecast smoothing, but it leads to a positive bias and makes HeatNet forecasts of negative anomalies extremely unlikely. The deviation of the forecast distribution from the true target PDF is further quantified in Figure 5 through the Kullback-Leibler (KL) divergence. The use of the symmetric exponential loss reduces the divergence of ExtNet to less than half of the GenNet divergence for all lead times, whereas the bias induced by the positive extreme loss results in a similar KL divergence compared to GenNet.

Although ExtNet does not manage to capture the same sharpness as the ECMWF ensemble, it is closer in KL divergence to it than to the MSE-trained GenNet model, highlighting the effectiveness of the exponential loss (2) in retaining forecast sharpness for a given architecture. Interestingly, the probability of strong positive anomaly forecasts with HeatNet, ExtNet and the ECMWF ensemble

mean in the extended range is roughly the same. This is in spite of very different probabilities of negative anomaly forecasts (Figure 4c).

d. Global surface temperature prediction skill

To further assess the effect of the exponential loss (2) on the general temperature prediction problem, we include in Figure 5 the RMSE and AnCC of T_{2m} (i.e., not standardized) for all dates in the test set, over both land and oceans. Note that the RMSE in this case is not debiased. Remarkably, NWMs trained using the exponential loss show a very small reduction in forecast skill in the general temperature prediction problem, particularly ExtNet. All NWMs beat persistence for all lead times and remain skillful with respect to the ECMWF control outside the medium range. The ECMWF ensemble mean remains the most skillful model beyond the short range, although the skill of ExtNet and GenNet is roughly similar after two weeks of lead time. Although the RMSE of ExtNet forecasts converges to that of climatology after three weeks, the model can forecast strong deviations from climatology, as shown in Figure 7 for an individual forecast at 23 days of lead time. Finally, the forecast biases of GenNet and ExtNet are similar in magnitude to those of the ECMWF model (Figure 5d), even though the neural weather predictions are not bias-corrected by reforecasts. We hypothesize that the small negative bias of ECMWF forecasts is due to the upwind nature of forecast calibration and the global warming trend. HeatNet does suffer from a significant positive bias, which explains its loss of RMSE_d skill in the heat prediction task with respect to ExtNet (Figure 3). From Figures 3–5, it is evident that ExtNet provides the best compromise between extreme heat forecasting skill, forecast reliability and surface temperature prediction accuracy among the NWMs considered.

Figure 5a also allows comparison with other NWMs in the literature. Weyn et al. (2021) use a neural network with a simpler albeit similar architecture as a time integrator, forecasting fields 6 and 12 hours into the future with each inference step. They show that only when taking an ensemble of such models can they beat the RMSE of the ECMWF S2S control forecast in the extended range. In contrast, producing all lead time predictions at once, we are able to beat the ECMWF control forecast both in RMSE and AnCC in the extended range. This is consistent with studies comparing direct and iterative forecasting using NWMs, which show that the former configuration leads to enhanced regressive skill (Rasp et al. 2020). The similarities between the ensemble forecast of

Weyn et al. (2021), the ECMWF ensemble, and our results, suggest that NWMs outputting longer lead times yield forecasts more similar to the ensemble mean of physics-driven forecasts than to a given physical trajectory.

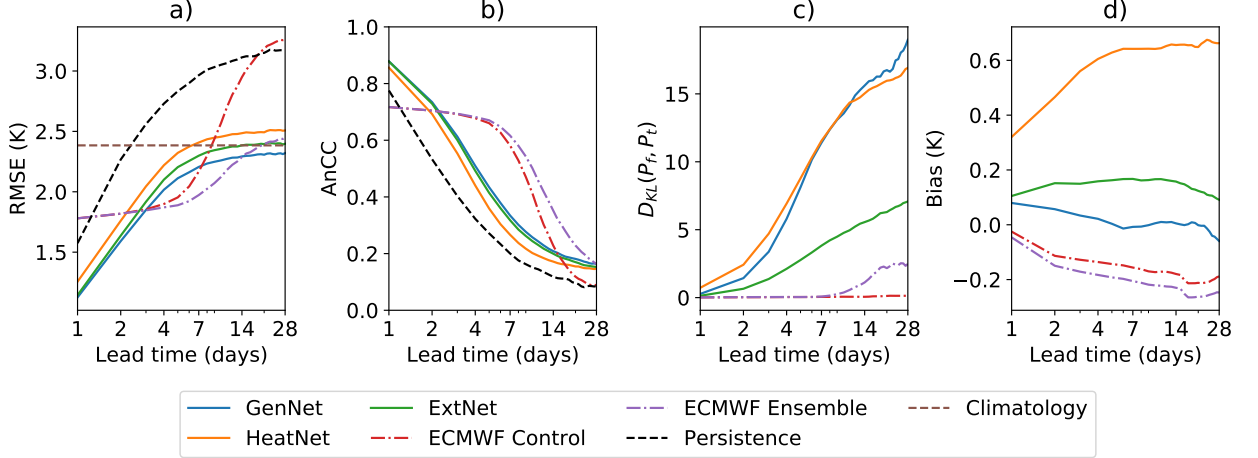


FIG. 5. Forecast metrics for the general 2 m temperature prediction task (T_{2m}), for different models as a function of lead time. From left to right, the root mean squared error (RMSE), the anomaly correlation coefficient (AnCC), the Kullback-Leibler divergence D_{KL} of \tilde{T}_{2m} with respect to the targets, and the unconditional T_{2m} bias. All results are global and temporal averages over the period 2017-2021. NWM names follow Section 2b.

The results in Figures 3-5 yield important insights into the questions that we posed in the introduction. NWMs trained on limited historical data can improve upon persistence in the prediction of out-of-sample rare events, in a regressive sense. However, for our chosen architecture, this can only be achieved when employing the exponential loss (2). Furthermore, training on the symmetric exponential loss, ExtNet is able to reduce the prediction error for extreme events and slow down the distributional shift with lead time, all while maintaining an unconditional regressive skill practically indistinguishable from models trained on the MSE. Finally, the extreme-focused models improve upon the ECMWF control forecasts in a regressive sense after two weeks, and rival the ECMWF ensemble mean in the extended range. We now explore two specific heatwave events as forecast by the ECMWF model and the NWMs to illustrate the implications of these results.

e. Analysis of the 2017 western European heatwave

Sections 4a and 4d highlight the different ways in which uncertainty affects physics-based and NWM forecasts. These differences are further explored here at the regional scale by considering the western European heatwave of June 2017. The 2017 heatwave resulted in the hottest June on record in Spain and the Netherlands, and the second warmest in France and Switzerland (Sánchez-Benítez et al. 2018). It was associated with northward warm air intrusions fostered by a subtropical ridge over western Europe, as shown by Sánchez-Benítez et al. (2018).

Forecasts of the standardized temperature anomaly on June 20, 2017 are shown in Figure 6 for several lead times. The ECMWF S2S control forecast initialized 5 days prior accurately predicted the spatial anomaly patterns over western Europe, slightly overpredicting their magnitude. It also overpredicted temperatures over Morocco. However, the forecast initialized on June 5 projected important negative temperature anomalies over most of western Europe, opposite of what was observed. It also failed to predict the northward warm air intrusion from the Saharan coast.

On the other hand, ExtNet robustly forecast the warm air intrusion for the same lead time (15 days), although not its northward penetration into France and the Benelux. At 5 days lead time, ExtNet predicted positive temperature anomalies over Europe, although milder than what was observed. This is due to the smoothing of NWM forecasts with lead time, as shown in Figures 6e and 6f. As expected from Figure 3, the NWM forecast one day ahead tracks well both the magnitude and patterns of temperature anomaly. In the medium and extended ranges, the forecast matches the temperature anomaly pattern well, but underestimates its magnitude.

f. Analysis of the 2021 western North American heatwave

Figure 6 is consistent with our hypothesis that, contrary to physics-based models, forecasts by the NWMs considered do not represent trajectories of the system. They are more closely related to the mean projection that one might obtain by performing an ensemble-based forecast with physics-based models, or NWMs acting as time integrators (Slingo and Palmer 2011; Weyn et al. 2021; Scher and Messori 2021). To further support this claim, we compare forecasts of the 2021 western North American (WNA) heatwave provided by ExtNet, GenNet and the ECMWF ensemble in Figure 7.

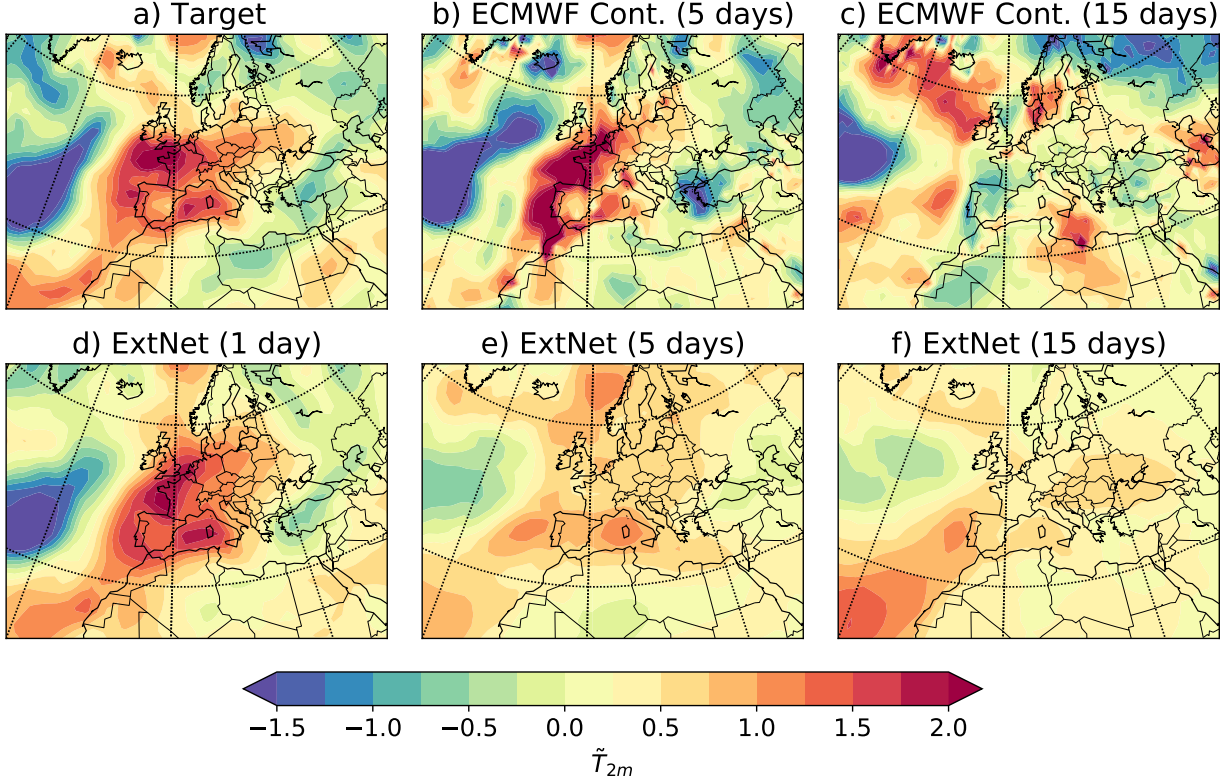


FIG. 6. Daily-averaged standardized 2-m temperature anomaly over Europe on June 20, 2017 from (a) the ERA5 reanalysis product, and as forecast by the ECMWF S2S control (ECMWF Cont.; b, c), and ExtNet (d, e, f). The lead time of the forecasts follows the title of each subfigure.

We consider the WNA heatwave because its forecast using state-of-the-art operational systems is well characterized in the literature (Lin et al. 2022). Several phenomena have been put forward as potential causes of the WNA heatwave. Lin et al. (2022) note the eastward propagation of a Rossby wave train from the tropical western Pacific that may have favored the formation of a heat dome over western North America. Mo et al. (2022) and Lin et al. (2022) also show that the heatwave was preceded by a strong atmospheric river transporting warm moist air from Southeast Asia into the region.

We focus on the heatwave onset, which took place June 25-26, 2021. The actual temperature anomaly on June 26 was characterized by heatwave conditions over Washington, Oregon and British Columbia. Extreme temperature anomalies were also observed over the northeastern Pacific and the Labrador Sea (Figure 7a). The ECMWF ensemble forecast from June 21 predicted

warm temperature anomalies over western North America, although smaller in magnitude than the reanalysis. The forecast from June 3, more than 3 weeks ahead, failed to predict positive anomalies over western North America or the Labrador Sea. This loss of predictive skill over land has been linked to the inability of the ECMWF ensemble to forecast both the continental penetration of the atmospheric river (Mo et al. 2022), and the eastward shift of the atmospheric ridge over western Canada (Lin et al. 2022).

ExtNet forecast the anomaly pattern correctly with 2 days of lead time, but only predicted significant positive anomalies over Washington, Oregon and the Labrador Sea in the forecast 5 days prior. Compared to GenNet, ExtNet provides significantly better and sharper forecasts for all lead times considered, confirming the results in Section 4a and 4c. GenNet underpredicted the extent of the heatwave over North America even in the short range, and failed to predict continental penetration 5 days prior to the event.

At 23 days of lead time, the ExtNet forecast closely resembles that of the ECMWF ensemble, exhibiting an anomaly dipole over the eastern Pacific (Figure 7c, f). Indeed, the data-driven model exhibits better correlation with the target over the Labrador Sea at this lead time, highlighting the skill of the model in the extended range. The resemblance of the ExtNet forecast to the ECMWF ensemble mean is consistent with our interpretation of the NWM forecasts as predictors of the mean physics-based trajectory.

5. Model interpretation

The NWMs presented here leverage a wider range of predictors than other extreme heat forecasting systems in the literature (Chattopadhyay et al. 2020; Jacques-Dumas et al. 2022). Here we assess the importance of the additional input fields using integrated gradients for feature attribution (Sundararajan et al. 2017; Sundararajan and Agrawal 2021).

a. Feature attribution through integrated gradients

The attribution for each feature $x^{(i)}$ is defined as the mean absolute value of its contribution to the model forecast $y' = \Psi(\theta^*, x)$ with respect to a null-contribution baseline forecast $y'_b = \Psi(\theta^*, x_b)$. We formulate the baseline input x_b to be the feature vector on the linear path between x_{\min} and x_{\max} that results in a forecast closest to global climatology ($y' \approx 0$), where x_{\min} and x_{\max} are feature

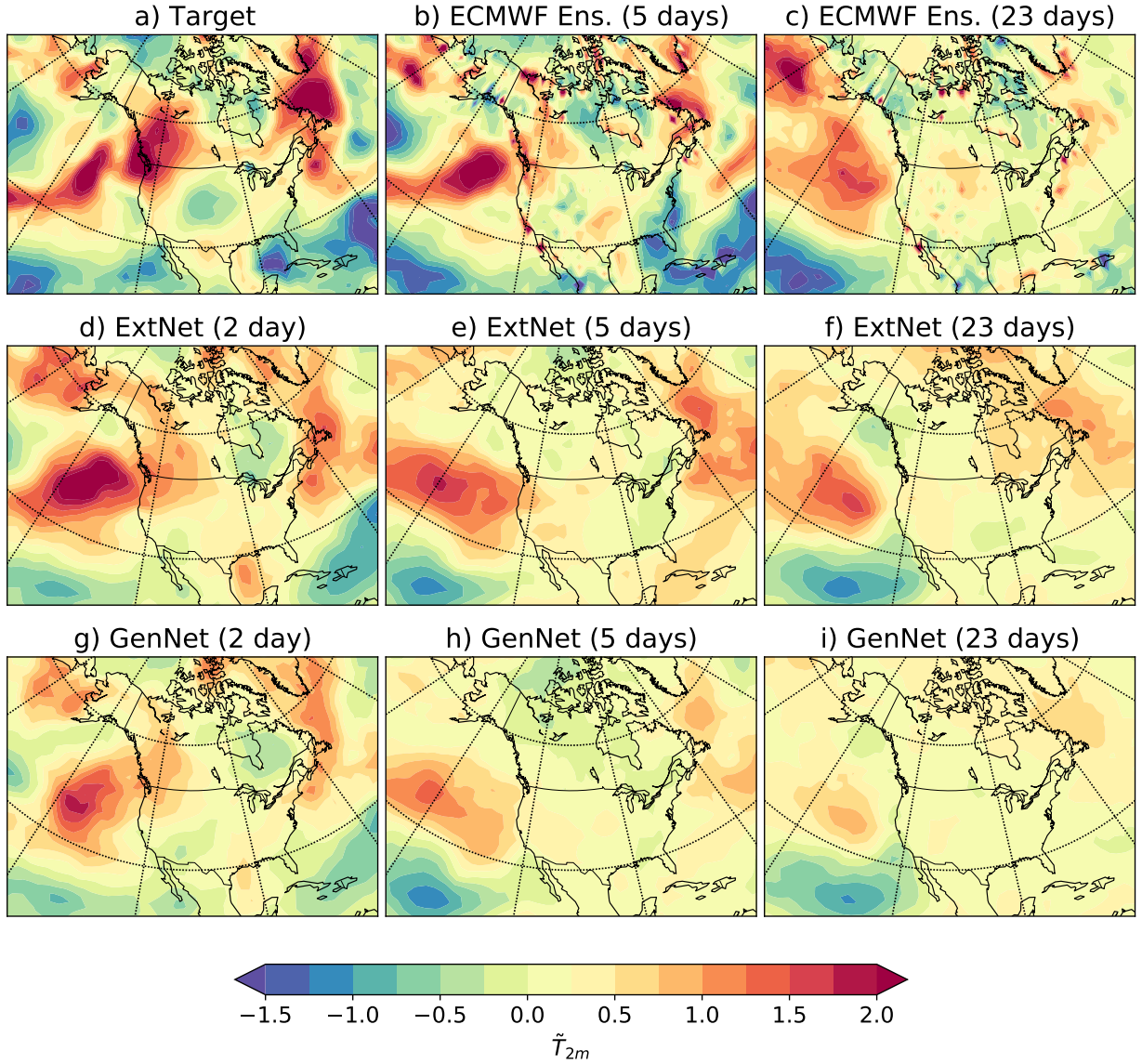


FIG. 7. Daily-averaged standardized 2-m temperature anomaly over North America on June 26, 2021 from (a) the ERA5 reanalysis product, and as forecast by the ECMWF perturbed ensemble mean (ECMWF Ens.; b, c), ExtNet (d, e, f) and GenNet (g, h, i). The lead time of the forecasts follows the title of each subfigure.

vectors constructed using the minimum and maximum values of the features found in the evaluation set, respectively.

For each actual forecast $y'_a = \Psi(\theta^*, x_a)$, the contribution is computed as the partial derivative of the forecast with respect to $x^{(i)}$, integrated along a linear path from the baseline $x_b = [x_b^{(1)}, x_b^{(2)}, \dots]^T$ to the actual input value $x_a = [x_a^{(1)}, x_a^{(2)}, \dots]^T$,

$$\text{Att}(x^{(i)})|_{y'_a} = \frac{1}{N} \left\| (x_a^{(i)} - x_b^{(i)}) \int_0^1 \frac{\delta \Psi(\theta^*, x(\alpha))}{\delta x^{(i)}} d\alpha \right\|_1, \quad (6)$$

where N is the number of pixels over which the L_1 -norm is computed, $\delta \Psi / \delta x^{(i)}$ is a discretized approximation of the partial derivative, and $\alpha \in [0, 1]$ parameterizes the linear path from baseline to actual feature values, such that $x(\alpha = 0) = x_b$ and $x(\alpha = 1) = x_a$. Finally, we compute the mean attribution for each feature over dates in the evaluation set.

b. Relevance of model inputs

We apply the integrated gradients methodology described in Section 5a to ExtNet forecasts for summer over land during the 5-year period from 2015 to 2019. Feature attributions are shown in Figure 8 for the extreme ($\tilde{T}_{2m} > 2$) and the general prediction task, for lead times spanning the short, medium and extended range. The contributions from the most recent data, data from the previous 2 days, and data from the first 4 days of the week preceding the forecast are shown in different colors to quantify the relevance of past history as a predictor of future states.

As expected, we find that \tilde{T}_{2m} itself is the most important feature in all cases, while the relevance of other features increases with forecast lead time and depends strongly on the task considered (i.e., extreme or general prediction). In addition, the relevance of feature history robustly increases with lead time, suggesting that NWM forecasts in the extended range learn to rely on lower-frequency signals.

In the extreme prediction task, the temperature anomaly, the 700 hPa geopotential height anomaly and the outgoing longwave radiation are important predictors at all lead times. Soil moisture below 7 cm gains relevance with lead time, consistent with the characteristic low frequency of land-atmosphere coupling processes and the memory of root-zone soil moisture (Wu et al. 2002). Additional relevant predictors include the potential vorticity at 500 hPa, and the geopotential height anomaly at 300 and 500 hPa. The potential vorticity at 700 hPa and the surface soil moisture above 7 cm are irrelevant to ExtNet predictions at all timescales.

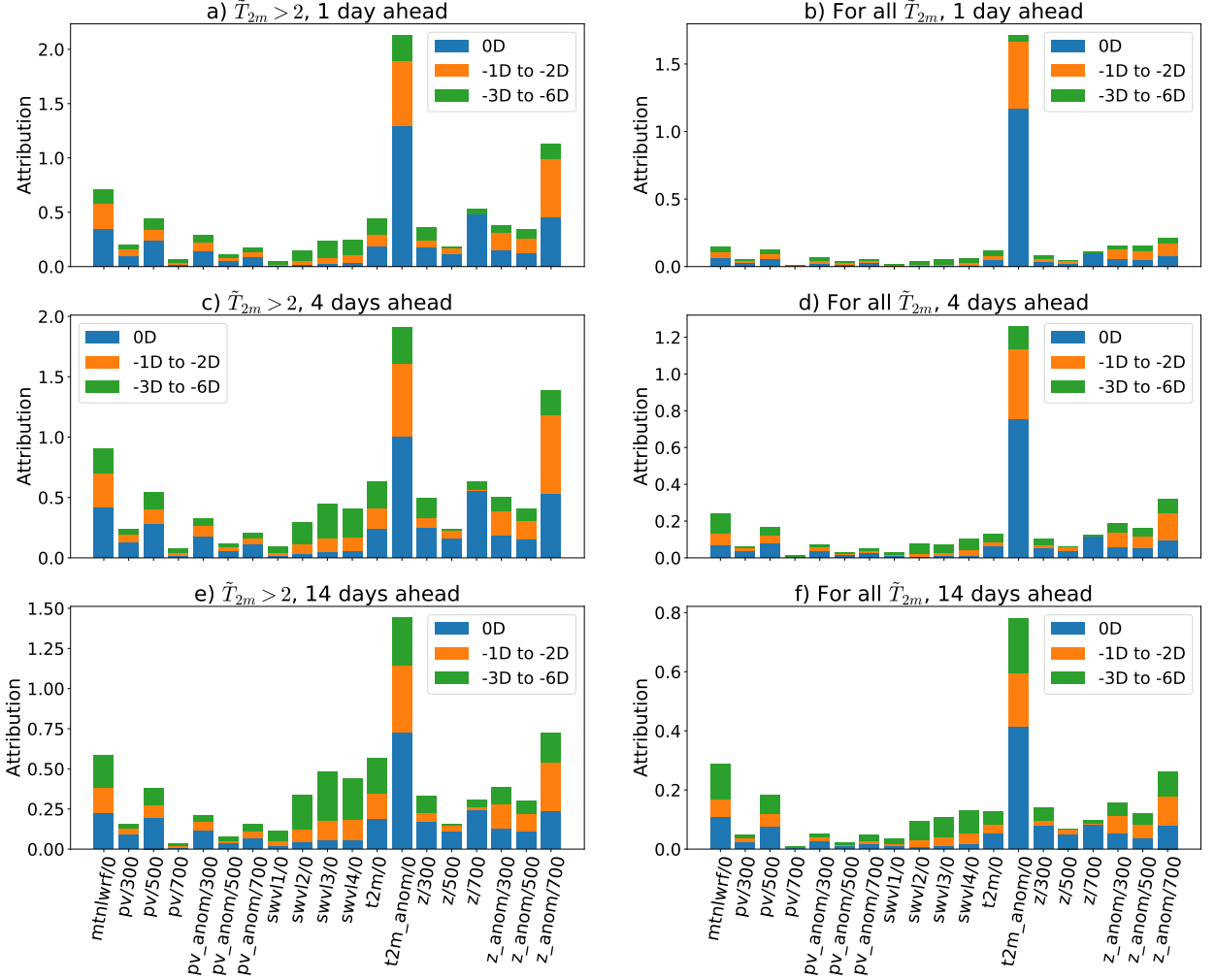


FIG. 8. Forecast feature attribution for summer over land, using data spanning the period 2015-2019. Attribution is shown for extreme and general prediction, and for different lead times. Feature names follow the notation *name/pressure level*, where each *name* follows ECMWF notation: *mtnlwrf* is outgoing longwave radiation, *pv* is potential vorticity, *z* is geopotential, *swvli* is soil water volume at level *i* below the ground, and *t2m* is temperature 2 m above the surface. The legend (*-iD*) defines the contribution of data *i* days before forecast initialization.

In the general prediction task, the 700 hPa geopotential height anomaly, the outgoing longwave radiation and the 500 hPa potential vorticity only become important after the first few days. Soil moisture plays a much smaller role in this task compared to heatwave prediction, consistent with observations of a much stronger land-atmosphere coupling under extreme conditions (Orth and Seneviratne 2012; Benson and Dirmeyer 2021). Regarding the auxiliary features, we find

topography to be the most relevant predictor, followed by the land sea mask, the insolation and the latitude. Contributions from the date and longitude were negligible in all cases. Overall, Figure 8 suggests that generic estimates of the relevance of alternative features for NWM forecasting may underestimate the contribution of such predictors to extreme event forecasting.

6. Discussion

Referencing the first question that we posed in the introduction, we find that deep learning systems trained on limited historical data can forecast out-of-sample extreme events with positive regressive skill above persistence for lead times between 1 and 28 days. An interesting research direction would be to train deep learning models using a much larger synthetic dataset as a first step (Chattopadhyay et al. 2020; Jacques-Dumas et al. 2022), and then leverage reanalysis products like ERA5 to fine-tune the model through transfer learning. This technique has already resulted in remarkable achievements in other fields of science, such as organic synthesis (Pesciullesi et al. 2020).

Regarding the second question, we find that NWMs trained on the mean squared error loss only marginally improve upon persistence for hot summer days, and fail to yield skillful forecasts of extremely hot days at any lead time considered, at least with our architecture and only using historical data. Our results suggest that it is crucial to train models using custom losses that emphasize extremes to achieve positive skill in this task, which has been shown before for idealized dynamical systems (Qi and Majda 2020). Moreover, the switch to the proposed symmetric exponential loss (2) with $(a, b) = (0.5, 0.5)$ results in negligible skill loss in the general temperature prediction problem, and yields reliable forecast distributions further into the future. Thus, the answer to our third question, whether NWMs trained to predict extremes retain skill in more general settings, is positive.

Our overall best neural weather model (ExtNet) compares favorably to the ECMWF S2S control forecast in the short and subseasonal range. In the extended range, ExtNet is able to yield lower errors and higher correlations with the target than the ECMWF S2S control, both in the general temperature prediction and extreme heat prediction tasks. This, however, does not fully translate into higher skill as a binary classifier due to the smoothness of forecasts with lead time. In the medium range, the ECMWF model remains the most powerful forecast system. The ECMWF

ensemble pushes the dominance of physics-based forecasts to longer lead times, but even then ExtNet retains regressive skill after three weeks. In the short range, the superiority of NWMs can be interpreted as the potential of physics-based systems to improve their short-range performance through better and faster data assimilation about the initial atmospheric state. This is another area where deep learning could accelerate progress.

Operational warning systems achieve maximal economic value when they can represent the space of possible trajectories as a probability density function, such that the occurrence of extreme events can be treated probabilistically, not as a binary problem (Palmer 2017). This is done in practice through the use of perturbed ensembles. The use of perturbed ensembles has recently been explored for NWMs acting as time-integrators (Scher and Messori 2021), which still show a moderate distributional shift with lead time (Weyn et al. 2021). The use of our proposed exponential loss may enable the use of longer time steps in iterative NWMs while preserving forecast sharpness.

An alternative avenue of research that may prove fruitful is the direct prediction of the probability distribution of trajectories (Sønderby et al. 2020), or some parametric approximation of it. In the context of climate modeling, Guillaumin and Zanna (2021) trained a convolutional neural network to predict the mean and standard deviation of subgrid-scale momentum fluxes in the ocean, which they parameterized as Gaussian. A similar approach could be taken to predict the ensemble spread in temperature anomaly projections, since direct deterministic NWM forecasts closely resemble a physics-based ensemble mean prediction. We hope that these and other methodologies, combined with the use of extreme-focused loss functions such as the one we propose, can enable reliable, actionable and efficient forecasting of extreme events using neural weather models in the near future.

Acknowledgments. The authors thank Stephan Hoyer, Tapio Schneider and John Anderson for valuable discussions that helped improve this paper. The authors also acknowledge the use of the DLWP-CS open source package developed by Jonathan Weyn as a starting point for this project.

Data availability statement. The ERA5 reanalysis data is freely available at the Copernicus Climate Data Store (<https://cds.climate.copernicus.eu>). The ECMWF S2S control and perturbed forecasts can be obtained from the Meteorological Archival and Retrieval System of ECMWF (<https://apps.ecmwf.int/datasets/data/s2s>). The software used to train the neural weather models is available on GitHub (<https://github.com/google-research/heatnet>).

APPENDIX A

Metric uncertainty estimation

The test set used in this article contains about 7 million samples, enough to render the uncertainty in metrics for the general prediction task negligible. This is no longer the case in the analysis of metrics during hot summer days over land. In that case, the metrics are computed over $> 70,000$ samples in the case of hot days ($\tilde{T}_{2m} > 1$) and $> 7,000$ samples in the case of extremely hot days ($\tilde{T}_{2m} > 2$). In order to determine the standard deviation of the sample mean due to finite sample size, we use block bootstrapping with year-long disjoint blocks (Hall et al. 1995). We construct the empirical distribution function of the sample mean from 10^6 bootstrap samples, and use its standard deviation as a measure of uncertainty. All uncertainty estimates proved robust to block size reduction except for EDI during extremely hot days and after a certain lead time for each NWM. Results are omitted for these EDI estimates in Figure 3.

References

- Benson, D. O., and P. A. Dirmeyer, 2021: Characterizing the relationship between temperature and soil moisture extremes and their role in the exacerbation of heat waves over the contiguous united states. *J. Clim.*, **34** (6), 2175–2187, <https://doi.org/10.1175/JCLI-D-20-0440.1>.
- Brás, T. A., J. Seixas, N. Carvalhais, and J. Jägermeyr, 2021: Severity of drought and heatwave crop losses tripled over the last five decades in europe. *Environmental Research Letters*, **16** (6), 065 012, <https://doi.org/10.1088/1748-9326/abf004>.

- Brenowitz, N. D., and C. S. Bretherton, 2018: Prognostic validation of a neural network unified physics parameterization. *Geophysical Research Letters*, **45**, 6289–6298, <https://doi.org/10.1029/2018GL078510>.
- Chattopadhyay, A., E. Nabizadeh, and P. Hassanzadeh, 2020: Analog forecasting of extreme-causing weather patterns using deep learning. *Journal of Advances in Modeling Earth Systems*, **12**, e2019MS001958, <https://doi.org/10.1029/2019MS001958>.
- Deng, K., M. Ting, S. Yang, and Y. Tan, 2018: Increased frequency of summer extreme heat waves over texas area tied to the amplification of pacific zonal SST gradient. *J. Clim.*, **31** (14), 5629–5647, <https://doi.org/10.1175/JCLI-D-17-0554.1>.
- ECMWF, 2016: *IFS Documentation CY43R1 - Part IV: Physical Processes*. No. 4, IFS Documentation, ECMWF, <https://doi.org/10.21957/sqvo5yxja>.
- ECMWF, 2019: *IFS Documentation CY46R1 - Part IV: Physical Processes*. No. 4, IFS Documentation, ECMWF, <https://doi.org/10.21957/xphfxep8c>.
- ECMWF, 2020: *IFS Documentation CY47R1 - Part IV: Physical Processes*. No. 4, IFS Documentation, ECMWF, <https://doi.org/10.21957/cpmkqvghja>.
- Espeholt, L., and Coauthors, 2021: Skillful twelve hour precipitation forecasts using large context neural networks. <https://doi.org/10.48550/arXiv.2111.07470>.
- Ferro, C. A. T., and D. B. Stephenson, 2011: Extremal dependence indices: Improved verification measures for deterministic forecasts of rare binary events. *Weather and Forecasting*, **26** (5), 699 – 713, <https://doi.org/10.1175/WAF-D-10-05030.1>.
- Guillaumin, A. P., and L. Zanna, 2021: Stochastic-deep learning parameterization of ocean momentum forcing. *Journal of Advances in Modeling Earth Systems*, **13**, e2021MS002534, <https://doi.org/10.1029/2021MS002534>.
- Hall, P., J. L. Horowitz, and B.-Y. Jing, 1995: On blocking rules for the bootstrap with dependent data. *Biometrika*, **82**, 561–574, <https://doi.org/10.2307/2337534>.
- He, K., X. Zhang, S. Ren, and J. Sun, 2015: Delving deep into rectifiers: Surpassing human-level performance on ImageNet classification. <https://doi.org/10.48550/arXiv.1502.01852>.

- Heo, S., M. L. Bell, and J.-T. Lee, 2019: Comparison of health risks by heat wave definition: Applicability of wet-bulb globe temperature for heat wave criteria. *Environmental Research*, **168**, 158–170, <https://doi.org/10.1016/j.envres.2018.09.032>.
- Hersbach, H., and Coauthors, 2020: The ERA5 global reanalysis. *Quarterly Journal of the Royal Meteorological Society*, **146** (730), 1999–2049, <https://doi.org/10.1002/qj.3803>.
- Huang, H., and Coauthors, 2020: UNet 3+: A Full-Scale connected UNet for medical image segmentation. <https://doi.org/10.48550/arXiv.2004.08790>, 2004.08790.
- Jacques-Coper, M., S. Brönnimann, O. Martius, C. S. Vera, and S. B. Cerne, 2015: Evidence for a modulation of the intraseasonal summer temperature in eastern patagonia by the Madden-Julian oscillation. *Journal of Geophysical Research: Atmospheres*, **120**, 7340–7357, <https://doi.org/10.1002/2014JD022924>.
- Jacques-Dumas, V., F. Ragone, P. Borgnat, P. Abry, and F. Bouchet, 2022: Deep learning-based extreme heatwave forecast. *Frontiers in Climate*, **4**, <https://doi.org/10.3389/fclim.2022.789641>.
- Ke, X., D. Wu, J. Rice, M. Kintner-Meyer, and N. Lu, 2016: Quantifying impacts of heat waves on power grid operation. *Applied Energy*, **183**, 504–512, <https://doi.org/10.1016/j.apenergy.2016.08.188>.
- Keisler, R., 2022: Forecasting global weather with graph neural networks. <https://doi.org/10.48550/arxiv.2202.07575>.
- Kingma, D. P., and J. Ba, 2017: Adam: A method for stochastic optimization. <https://doi.org/10.48550/arXiv.1412.6980>, 1412.6980.
- Lin, H., R. Mo, and F. Vitart, 2022: The 2021 western North American heatwave and its subseasonal predictions. *Geophysical Research Letters*, **49**, e2021GL097036, <https://doi.org/10.1029/2021GL097036>.
- Lopez-Gomez, I., Y. Cohen, J. He, A. Jaruga, and T. Schneider, 2020: A generalized mixing length closure for eddy-diffusivity mass-flux schemes of turbulence and convection. *Journal of Advances in Modeling Earth Systems*, **12**, e2020MS002161, <https://doi.org/10.1029/2020MS002161>.

- Lorenz, E. N., 1969a: Atmospheric predictability as revealed by naturally occurring analogues. *Journal of Atmospheric Sciences*, **26**, 636–646, [https://doi.org/10.1175/1520-0469\(1969\)26<636:APARBN>2.0.CO;2](https://doi.org/10.1175/1520-0469(1969)26<636:APARBN>2.0.CO;2).
- Lorenz, E. N., 1969b: The predictability of a flow which possesses many scales of motion. *Tellus*, **21** (3), 289–307, <https://doi.org/10.1111/j.2153-3490.1969.tb00444.x>.
- Maloney, E. D., Ángel F Adames, and H. X. Bui, 2019: Madden–Julian oscillation changes under anthropogenic warming. *Nature Climate Change*, **9**, 26–33, <https://doi.org/10.1038/s41558-018-0331-6>.
- Mann, M. E., S. Rahmstorf, K. Kornhuber, B. A. Steinman, S. K. Miller, S. Petri, and D. Coumou, 2018: Projected changes in persistent extreme summer weather events: The role of quasi-resonant amplification. *Science advances*, **4**, eaat3272–eaat3272, <https://doi.org/10.1126/sciadv.aat3272>.
- Miller, D. E., Z. Wang, B. Li, D. S. Harnos, and T. Ford, 2021: Skillful subseasonal prediction of U.S. extreme warm days and standardized precipitation index in boreal summer. *J. Clim.*, **34** (14), 5887–5898, <https://doi.org/10.1175/JCLI-D-20-0878.1>.
- Mo, R., H. Lin, and F. Vitart, 2022: An anomalous atmospheric river linked to the late June 2021 western North America heatwave. Research Square Platform LLC, <https://doi.org/10.21203/rs.3.rs-1125330/v1>.
- Ogi, M., Y. Tachibana, and K. Yamazaki, 2003: Impact of the wintertime north Atlantic oscillation (NAO) on the summertime atmospheric circulation. *Geophysical Research Letters*, **30**, <https://doi.org/10.1029/2003GL017280>.
- Orth, R., and S. I. Seneviratne, 2012: Analysis of soil moisture memory from observations in Europe. *Journal of Geophysical Research: Atmospheres*, **117**, <https://doi.org/10.1029/2011JD017366>.
- Palmer, T., 2017: The primacy of doubt: Evolution of numerical weather prediction from determinism to probability. *Journal of Advances in Modeling Earth Systems*, **9** (2), 730–734, <https://doi.org/10.1002/2017MS000999>.

- Palmer, T. N., 1993: Extended-range atmospheric prediction and the Lorenz model. *Bulletin of the American Meteorological Society*, **74**, 49–66, [https://doi.org/10.1175/1520-0477\(1993\)074<0049:ERAPAT>2.0.CO;2](https://doi.org/10.1175/1520-0477(1993)074<0049:ERAPAT>2.0.CO;2).
- Parente, J., M. Pereira, M. Amraoui, and E. Fischer, 2018: Heat waves in Portugal: Current regime, changes in future climate and impacts on extreme wildfires. *Science of The Total Environment*, **631–632**, 534–549, <https://doi.org/10.1016/j.scitotenv.2018.03.044>.
- Pathak, J., and Coauthors, 2022: FourCastNet: A global data-driven high-resolution weather model using adaptive fourier neural operators. <https://doi.org/10.48550/arxiv.2202.11214>.
- Perkins-Kirkpatrick, S. E., and S. C. Lewis, 2020: Increasing trends in regional heatwaves. *Nature Communications*, **11**, 3357, <https://doi.org/10.1038/s41467-020-16970-7>.
- Pesciullesi, G., P. Schwaller, T. Laino, and J.-L. Reymond, 2020: Transfer learning enables the molecular transformer to predict regio- and stereoselective reactions on carbohydrates. *Nature Communications*, **11**, 4874, <https://doi.org/10.1038/s41467-020-18671-7>.
- Qi, D., and A. J. Majda, 2020: Using machine learning to predict extreme events in complex systems. *Proceedings of the National Academy of Sciences*, **117** (1), 52–59, <https://doi.org/10.1073/pnas.1917285117>.
- Rasp, S., P. D. Dueben, S. Scher, J. A. Weyn, S. Mouatadid, and N. Thuerey, 2020: WeatherBench: A benchmark data set for data-driven weather forecasting. *Journal of Advances in Modeling Earth Systems*, **12**, e2020MS002 203, <https://doi.org/10.1029/2020MS002203>.
- Ravuri, S., and Coauthors, 2021: Skilful precipitation nowcasting using deep generative models of radar. *Nature*, **597**, 672–677, <https://doi.org/10.1038/s41586-021-03854-z>.
- Richardson, D. S., 2000: Skill and relative economic value of the ECMWF ensemble prediction system. *Quarterly Journal of the Royal Meteorological Society*, **126**, 649–667, <https://doi.org/10.1002/qj.49712656313>.
- Robine, J.-M., S. L. K. Cheung, S. Le Roy, H. Van Oyen, C. Griffiths, J.-P. Michel, and F. R. Herrmann, 2008: Death toll exceeded 70,000 in europe during the summer of 2003. *Comptes Rendus Biologies*, **331** (2), 171–178, <https://doi.org/10.1016/j.crv.2007.12.001>.

- Ronchi, C., R. Iacono, and P. S. Paolucci, 1996: The “cubed sphere”: A new method for the solution of partial differential equations in spherical geometry. *Journal of Computational Physics*, **124**, 93–114, <https://doi.org/10.1006/jcph.1996.0047>.
- Ronneberger, O., P. Fischer, and T. Brox, 2015: U-Net: Convolutional networks for biomedical image segmentation. *Medical Image Computing and Computer-Assisted Intervention – MICCAI 2015*, N. Navab, J. Hornegger, W. M. Wells, and A. F. Frangi, Eds., Springer International Publishing, Cham, 234–241, https://doi.org/10.1007/978-3-319-24574-4_28.
- Ruffault, J., and Coauthors, 2020: Increased likelihood of heat-induced large wild-fires in the mediterranean basin. *Scientific Reports*, **10**, 13 790, <https://doi.org/10.1038/s41598-020-70069-z>.
- Scher, S., and G. Messori, 2021: Ensemble methods for neural network-based weather forecasts. *Journal of Advances in Modeling Earth Systems*, **13**, <https://doi.org/10.1029/2020MS002331>.
- Slingo, J., and T. Palmer, 2011: Uncertainty in weather and climate prediction. *Philosophical Transactions of the Royal Society A: Mathematical, Physical and Engineering Sciences*, **369** (1956), 4751–4767, <https://doi.org/10.1098/rsta.2011.0161>.
- Sundararajan, M., and S. Agrawal, 2021: The rain check. *4th Workshop on Visualization for AI Explainability*, URL <http://raincheck.karyk.com/rain-check>.
- Sundararajan, M., A. Taly, and Q. Yan, 2017: Axiomatic attribution for deep networks. <https://doi.org/10.48550/arxiv.1703.01365>.
- Sánchez-Benítez, A., R. García-Herrera, D. Barriopedro, P. M. Sousa, and R. M. Trigo, 2018: June 2017: The earliest European summer mega-heatwave of reanalysis period. *Geophysical Research Letters*, **45**, 1955–1962, <https://doi.org/10.1002/2018GL077253>.
- Sønderby, C. K., and Coauthors, 2020: MetNet: A neural weather model for precipitation forecasting. arXiv, <https://doi.org/10.48550/ARXIV.2003.12140>.
- Teng, H., G. Branstator, H. Wang, G. A. Meehl, and W. M. Washington, 2013: Probability of US heat waves affected by a subseasonal planetary wave pattern. *Nat. Geosci.*, **6** (12), 1056–1061, <https://doi.org/10.1038/ngeo1988>.

- Ullrich, P. A., D. Devendran, and H. Johansen, 2016: Arbitrary-order conservative and consistent remapping and a theory of linear maps: Part II. *Monthly Weather Review*, **144** (4), 1529 – 1549, <https://doi.org/10.1175/MWR-D-15-0301.1>.
- Ullrich, P. A., and M. A. Taylor, 2015: Arbitrary-order conservative and consistent remapping and a theory of linear maps: Part I. *Monthly Weather Review*, **143** (6), 2419 – 2440, <https://doi.org/10.1175/MWR-D-14-00343.1>.
- Vautard, R., and Coauthors, 2007: Summertime European heat and drought waves induced by wintertime mediterranean rainfall deficit. *Geophysical Research Letters*, **34**, <https://doi.org/10.1029/2006GL028001>.
- Vitart, F., and Coauthors, 2017: The subseasonal to seasonal (S2S) prediction project database. *Bulletin of the American Meteorological Society*, **98**, 163–173, <https://doi.org/10.1175/BAMS-D-16-0017.1>.
- Wang, G., A. J. Dolman, and A. Alessandri, 2011: A summer climate regime over Europe modulated by the north Atlantic oscillation. *Hydrology and Earth System Sciences*, **15**, 57–64, <https://doi.org/10.5194/hess-15-57-2011>.
- Weyn, J. A., D. R. Durran, and R. Caruana, 2020: Improving data-driven global weather prediction using deep convolutional neural networks on a cubed sphere. *Journal of Advances in Modeling Earth Systems*, **12**, e2020MS002 109, <https://doi.org/10.1029/2020MS002109>.
- Weyn, J. A., D. R. Durran, R. Caruana, and N. Cresswell-Clay, 2021: Sub-Seasonal Forecasting With a Large Ensemble of Deep-Learning Weather Prediction Models. *Journal of Advances in Modeling Earth Systems*, **13** (7), e2021MS002 502, <https://doi.org/10.1029/2021MS002502>.
- White, C. J., and Coauthors, 2017: Potential applications of subseasonal-to-seasonal (S2S) predictions. *Meteorological Applications*, **24**, 315–325, <https://doi.org/10.1002/met.1654>.
- White, R. H., K. Kornhuber, O. Martius, and V. Wirth, 2021: From Atmospheric Waves to Heatwaves: A Waveguide Perspective for Understanding and Predicting Concurrent, Persistent and Extreme Extratropical Weather. *Bulletin of the American Meteorological Society*, 1–35, <https://doi.org/10.1175/BAMS-D-21-0170.1>.

- Wilks, D. S., 2019: *Statistical Methods in the Atmospheric Sciences*. 4th ed., Elsevier, 369-483 pp., <https://doi.org/10.1016/B978-0-12-815823-4.00009-2>.
- Wright, C. K., K. M. de Beurs, and G. M. Henebry, 2014: Land surface anomalies preceding the 2010 Russian heat wave and a link to the north Atlantic oscillation. *Environmental Research Letters*, **9**, 124 015, <https://doi.org/10.1088/1748-9326/9/12/124015>.
- Wu, W., M. A. Geller, and R. E. Dickinson, 2002: The Response of Soil Moisture to Long-Term Variability of Precipitation. *Journal of Hydrometeorology*, **3** (5), 604–613, [https://doi.org/10.1175/1525-7541\(2002\)003<0604:TROSMT>2.0.CO;2](https://doi.org/10.1175/1525-7541(2002)003<0604:TROSMT>2.0.CO;2).
- Wulff, C. O., and D. I. V. Domeisen, 2019: Higher subseasonal predictability of extreme hot European summer temperatures as compared to average summers. *Geophysical Research Letters*, **46**, 11 520–11 529, <https://doi.org/10.1029/2019GL084314>.
- Xu, Z., G. FitzGerald, Y. Guo, B. Jalaludin, and S. Tong, 2016: Impact of heatwave on mortality under different heatwave definitions: A systematic review and meta-analysis. *Environment International*, **89-90**, 193–203, <https://doi.org/10.1016/j.envint.2016.02.007>.
- Yu, F., and V. Koltun, 2016: Multi-scale context aggregation by dilated convolutions. *4th International Conference on Learning Representations, ICLR 2016, San Juan, Puerto Rico, May 2-4, 2016, Conference Track Proceedings*, Y. Bengio, and Y. LeCun, Eds., <https://doi.org/10.48550/arXiv.1511.07122>.